Synaptic dependence of dynamic regimes when coupling neural populations

Roberto Barrio,[1, *] Jorge A. Jover-Galtier,[1] Ana Mayora-Cebollero,[1] Carmen Mayora-Cebollero,[1] and Sergio Serrano[1]

[1]*Department of Applied Mathematics and IUMA. Computational Dynamics group. University of Zaragoza. E-50009. Spain.*
(Dated: February 4, 2024)

In this article we focus on the study of the collective dynamics of neural networks. The analysis of two recent models of coupled "next-generation" neural mass models allows us to observe different global mean dynamics of large neural populations. These models describe the mean dynamics of all-to-all coupled networks of quadratic integrate-and-fire spiking neurons. In addition, one of these models considers the influence of the synaptic adaptation mechanism on the macroscopic dynamics. We show how both models are related through a parameter and we study the evolution of the dynamics when switching from one model to the other by varying that parameter. Interestingly, we have detected three main dynamical regimes in the coupled models: Rössler-type (funnel type), bursting-type, and spiking-like (oscillator-type) dynamics. This result opens the question of which regime is the most suitable for realistic simulations of large neural networks and shows the possibility of the emergence of chaotic collective dynamics when synaptic adaptation is very weak.

Understanding how the brain works is one of the main goals of current science. Synchronization in large populations of neurons has been shown to be directly related to different brain functions and dysfunctions. Indeed, the ubiquity of oscillations in the brain supports the hypothesis that some cognitive functions require rhythmic firing patterns [1]. However, the dynamical analysis of large neural networks is a complex task. In recent years, different studies have been carried out to establish mean-field theories, which provide low-dimensional systems that give information on the global dynamics of neural populations [2–6] and are accurate in the thermodynamic limit (for large numbers of neurons).

In theoretical neuroscience, simple coupled mean-field models have recently been studied to localize macroscopic coherence states (phase-locking) in which global gamma-band oscillations arise [7–9]. It is interesting to note how macroscopic oscillations within different brain regions can show different phase-locks [10]. Different experimental and numerical results show how two oscillating neural groups communicate more efficiently when they maintain a phase-locked state: they can send information consecutively during the most excitable phase of the postsynaptic rhythm [11]. For example, these couplings are crucial for current theories of how oscillations shape the information transfer within and across the cortex, what is called the communication through coherence hypothesis [11]. Thus, experimental data exist to support the existence of multiple modes of phase-locking in the brain, but the main mechanisms that enable phase-locking of macroscopic rhythms need to be studied. Therefore, in this article we focus on some basic mathematical models of coupled neural populations to study the emergent macroscopic phase-locking within the theoretical framework of weakly coupled oscillators (simple quadratic integrate-and-fire neural models).

Another question is what type of phase locking can appear and whether this locking is with or without delay. In fact, a functionally optimal locking mode does not always have zero phase delay because the transmission of spikes from one area of the brain (a network) to another is not instantaneous and can take up to hundreds of milliseconds [12] depending on distance. Actually, recent experimental studies [13] have demonstrated a multiplicity of phase differences and have suggested that this fact could facilitate information selectivity [14]. Therefore, studying what synaptic mechanisms and what mathematical models can generate different coordinated rhythms is a relevant task and can shed light on the understanding of its functional role [15].

Two recent simple mathematical models that consider synaptic adaptation are the models of Dumont and Gutkin [7] and Ferrara *et al.* [9, 16]. In the first, the authors consider variations in synaptic currents, and it is the model that we will use since it connects with the well-known Montbrió *et al.* [17] mean-field model. The other model uses spike rate adaptation, which is a neural mechanism that considers the reduction of firing activity due to spike peaks. In recent publications [9, 18, 19] the authors have studied the effect of spike frequency adaptation on the macroscopic dynamics of coupled quadratic integrate-and-fire neural populations that integrate and activate. Interestingly, in [9] it has recently been shown that the addition of spike frequency adaptation leads to new collective dynamic regimes that resemble spiking or bursting dynamics of an isolated neuron [20]. Tonic spiking at the macroscopic level may correspond to periodic collective oscillations (phase-locked periodic state). Note that networks of identical spiking neurons in the absence of noise with purely excitatory activity [21] or inhibitory interactions [22] can exhibit this behavior. On the other hand, the bursting dynamics corresponds to a relaxation oscillation that links a spiking regime to a quiescence state (state of inactivity).

Periodic collective oscillations appear naturally when long decay times of synaptic conductances are used in inhibitory quadratic integrate-and-fire networks, and the main mechanism is through a Hopf bifurcation such as in the mean-field model considered in [18, 23]. The appearance of bursting behaviors in neural mass models may be an interesting task due to the option to generate more dynamical behaviors to the network, and the results of the experiments suggest that cholinergic drugs may be responsible for a modification of the frequency of neural oscillations and can cause different changes [24–28].

Therefore, the main objective of this article is to show how

collective spiking or bursting regimes appear in neural mass models, and whether another type of regime is also present.

In this paper we study two mean-field models (MPR and DG models introduced in [17] and [7], respectively) designed to describe all-to-all coupled networks of quadratic integrate-and-fire (QIF) neurons. The MPR model of Montbrió *et al.* [17] describes the macroscopic dynamics of a population of fully coupled QIF neurons using instantaneous synapses, while the DG model of Dumont and Gutkin [7] takes into account variations in synaptic currents. These models will be applied to a system of two coupled networks, one of them excitatory (with N_e neurons) and the other inhibitory (with N_i neurons). We have chosen these two models because the MPR model is a well-known neural mean-field model in the mathematical neuroscience and Kuramoto model communities. The article [17] was relevant as it was one of the first mean-field models of QIF neurons that used the Ott-Antonsen ansatz [29] (widely used in Kuramoto-type models). The choice of the DG model was due to the fact that we observed that it is a generalization of the MPR model and introduces synaptic adaptability. The use of simplified mathematical models has already received attention in computational neuroscience due to the possibility of performing more detailed analyses [6, 30–33]. A complete study of all the collective dynamics is an open task and we intend to focus on this problem as well as to locate some of the different dynamics in a parameter phase space.

The MPR mean-field equations for two coupled populations (one excitatory and the other inhibitory) [17] are

$$
\begin{cases}
\tau_e \dot{r}_e = \dfrac{\Delta_e}{\pi \tau_e} + 2 r_e v_e, \\[2mm]
\tau_e \dot{v}_e = v_e^2 + \bar{\eta}_e - (\tau_e \pi r_e)^2 + \tau_e J_{ee} r_e - \tau_e J_{ei} r_i + I_e^{ext}, \\[2mm]
\tau_i \dot{r}_i = \dfrac{\Delta_i}{\pi \tau_i} + 2 r_i v_i, \\[2mm]
\tau_i \dot{v}_i = v_i^2 + \bar{\eta}_i - (\tau_i \pi r_i)^2 + \tau_i J_{ie} r_e - \tau_i J_{ii} r_i + I_i^{ext}.
\end{cases}
\tag{1}
$$

The variables r_* and v_* represent, respectively, the firing rate and the mean voltage of the excitatory ($* = e$) and inhibitory population ($* = i$). The model parameters are: J_* ($* \in \{ee, ei, ie, ii\}$), the synaptic strengths of the connections; I_*^{ext} ($* \in \{e, i\}$), the external inputs; and Δ_* and $\bar{\eta}_*$ ($* \in \{e, i\}$), the half-width and the mean value (in the Cauchy sense) of a Lorentzian distribution used to achieve network heterogeneity. τ_e and τ_i are the membrane time constants and, for this model, we consider them equal to 1 as in the original equations of [17].

The MPR mean-field equations (1) are deduced from the following voltage equations [17] (for the neurons of the excitatory and inhibitory population, respectively):

$$
\begin{cases}
\dot{v}_{e,j} = v_{e,j}^2 + \eta_{e,j} + J_{ee} r_e - J_{ei} r_i + I_e^{ext}, \\
\dot{v}_{i,k} = v_{i,k}^2 + \eta_{i,k} + J_{ie} r_e - J_{ii} r_i + I_i^{ext},
\end{cases}
$$

where $j = 1, ..., N_e$ and $k = 1, ..., N_i$. Notice that $(\eta_{e,j}, \eta_{i,k})$ are the Lorentzian distributed constant currents. The following

formula corresponds to the Lorentzian distribution [16] (Δ_* and $\bar{\eta}_*$ are the half-width and the mean value of the named distribution):

$$
\mathscr{L}(\eta_*) = \frac{\Delta_*}{\pi[(\eta_* - \bar{\eta}_*)^2 + \Delta_*^2]}.
$$

More information about these equations (and the ones used to deduce the following equations (2)) can be found in Appendix.

For the case of the DG model, the mean-field equations for two coupled populations (one excitatory and the other inhibitory) [7] are

$$
\begin{cases}
\tau_e \dot{r}_e = \dfrac{\Delta_e}{\pi \tau_e} + 2 r_e v_e, \\[2mm]
\tau_e \dot{v}_e = v_e^2 + \bar{\eta}_e - (\tau_e \pi r_e)^2 + \tau_e S_{ee} - \tau_e S_{ei} + I_e^{ext}, \\[2mm]
\tau_{Se} \dot{S}_{ee} = -S_{ee} + J_{ee} r_e, \\[2mm]
\tau_{Si} \dot{S}_{ei} = -S_{ei} + J_{ei} r_i, \\[2mm]
\tau_i \dot{r}_i = \dfrac{\Delta_i}{\pi \tau_i} + 2 r_i v_i, \\[2mm]
\tau_i \dot{v}_i = v_i^2 + \bar{\eta}_i - (\tau_i \pi r_i)^2 + \tau_i S_{ie} - \tau_i S_{ii} + I_i^{ext}, \\[2mm]
\tau_{Se} \dot{S}_{ie} = -S_{ie} + J_{ie} r_e, \\[2mm]
\tau_{Si} \dot{S}_{ii} = -S_{ii} + J_{ii} r_i.
\end{cases}
\tag{2}
$$

where the same variables and parameters are used as in (1), along with the variables S_* ($* \in \{ee, ei, ie, ii\}$) that represent the synaptic currents between connections, and the parameters τ_{S_*} ($* \in \{e, i\}$) are the synaptic time constants of the connections.

Figure 1 shows a comparison between the mean-field model (1) and the average of a full system simulation of two coupled populations with 50,000 neurons each (see the Appendix for more details about the simulation of the complete network). Panels (A) and (B) show the neurons in the excitatory and inhibitory population, respectively, that are active at each time step. Panels (C) and (D) display how the firing rate and voltage of the excitatory population for the mean-field model are very similar to the average firing rate and voltage calculated when the entire system of neurons is simulated. All system variables, and not just the firing rate, are accurately described by the mean-field model. Panels (E) and (F) show the results for the inhibitory population. These results support the validity of mean-field approximations for the description of large populations of neurons and, in particular, for the systems of interest in this article.

We have introduced the two mean-field models (MPR (1) and DG (2)) that we analyze in this article. These models describe two coupled populations of QIF neurons. The main difference between both models is that the MPR model (1) only involves the strength of synaptic connections (between neurons of the same population or between both populations), while the DG model (2) also includes the change in synaptic currents. This fact is relevant, since it takes into account the possibility of neural synaptic adaptation [19]. Note that, when $\tau_{S_e} = \tau_{S_i} = 0$ and $\tau_e = \tau_i = 1$, both models are identical; then,
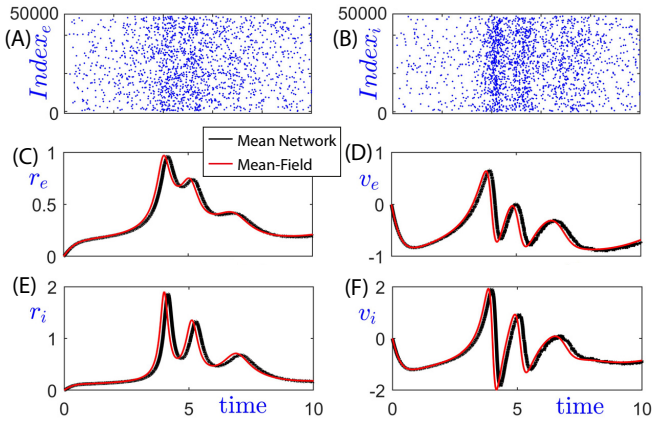
FIG. 1: Results of the mean-field MPR model (1) for two coupled populations and the complete simulation of said populations, with parameters $N_e = N_i = 50,000$; $\Delta_e = \Delta_i = 1$; $J_{ee} = J_{ie} = 18$; $J_{ei} = 6$; $J_{ii} = 0$; $\bar{\eta}_e = -2.526$; $\bar{\eta}_i = -4$; and $I_e^{ext}(t) = I_i^{ext}(t) = 0$ (which correspond to the first 10ms of the green point parameter values of Figure 4). The initial conditions for all variables are 0. The threshold and reset values for the voltage used to illustrate the behavior of the mean-field network are 100 and -100, respectively. (A) and (B) Activation of $50,000$ neurons (randomly ordered) from the excitatory and inhibitory populations, respectively, in the full simulation with respect to time. (C) and (D) Red: firing rate and voltage of the excitatory population in the mean-field model. Black: average firing rate and voltage of the excitatory population in the full simulation. (E) and (F) Red: Firing rate and voltage of the inhibitory population in the mean-field model. Black: average firing rate and voltage of the inhibitory population in the full simulation.

the MPR model is a limit case of the DG model. Therefore, an important question is: how does the dynamics change from one model to another when τ_{S_e} and τ_{S_i} vary?

To compare both models, we will consider $\tau_e = \tau_i = 1$ and $\tau_{S_e} = \tau_{S_i}$. To simplify the notation, from now on we will use $\tau_S := \tau_{S_e} = \tau_{S_i}$ as the new parameter. Since the case $\tau_S = 0$ in (2) corresponds to the MPR model, we now have a single parameter connecting the two models. Additionally, below, we will set the following values for the parameters: $\Delta_e = \Delta_i = 1$, $I_e^{ext} = I_i^{ext} = 0$, $J_{ee} = J_{ie} = 18$, $J_{ei} = 6$, $J_{ii} = 0$; leaving $\bar{\eta}_e$ and $\bar{\eta}_i$ as free parameters. In panels (A1) and (A2) of Figure 2, the projections in the plane (r_i, v_i) of the attractors for the MPR model ($\tau_S = 0$) and the DG model with $\tau_S = 1$ are represented, both calculated for $\bar{\eta}_e = -2.41$ and $\bar{\eta}_i = -4.005$. As can be seen, the dynamics of both attractors is very different. In the case $\tau_S = 0$ (A1), the attractor appears to be chaotic with funnel-type dynamics (Rössler-type [34, 35]). In contrast, the attractor for $\tau_S = 1$ (A2) is a periodic orbit with small oscillations on an upper plateau (in the central time series (A3) you can clearly see this bursting-type dynamics [36]). Figure 2 motivates an in-depth analysis of the dominant dynamics in each of the two models for a broader range of values of $\bar{\eta}_e$ and $\bar{\eta}_i$.

Figures 3 and 4 show a comparison between the MPR model (1) and the DG model (2) with $\tau_S = 1$. The panels Figure 3(A) and Figure 4(A) show their respective biparametric
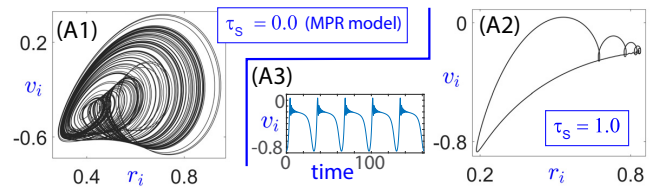
FIG. 2: Orbits of the mean-field equations, showing changes in dynamics for different values of the synaptic parameter τ_S. The initial conditions are $(r_e, v_e, r_i, v_i, S_{ee}, S_{ei}, S_{ie}, S_{ii}) = (1, -1, 1, -1, 1, 1, 1, 1)$. (A1) Orbit of the MPR model (1), equivalent to the DG model (2) for $\tau_S = 0$. (A2) and (A3) Orbit of the DG model (2) for $\tau_S = 1$.

plates obtained with the spike-counting technique [37] over the parameter space $\bar{\eta}_e \in [-2.7, -2.35]$, $\bar{\eta}_i \in [-4.5, -3.5]$ with the remaining parameters set as above. The colors represent the number of cuts of orbits with the Poincaré section $\prod_* := \{\mathbf{x} \in \mathbb{R}^{n_*} : \dot{v}_i = 0 \wedge \ddot{v}_i < 0\}$ ($* \in \{MPR, DG\}$, $n_{MPR} = 4$, $n_{DG} = 8$); that is, spikes are identified as relative maxima for the variable v_i over a period (more details in the Appendix). A maximum value of 8 peaks has been considered to facilitate the identification of areas with a reduced number of spikes, although the regions marked with the maximum in many cases have many more spikes than indicated (we will return to this later). These plates show two outer regions in dark blue (top left and bottom right) corresponding to 0 spikes, representing dynamics heading towards a stable equilibrium point. In the central area, different regions with different numbers of spikes indicate periodic or chaotic attractors. For both values of τ_s, the line $\bar{\eta}_i = -4.0$ crosses regions with attractors of different nature; the remaining panels illustrate different aspects of the dynamics of that uniparametric line.

Let us start by analyzing how the dynamics of the DG model for $\tau_S = 1$ varies along the selected parametric line $\bar{\eta}_i = -4.0$. Starting from the upper left outer region in panel Figure 3(A) and moving towards the inner region, the equilibrium point loses its stability due to a Hopf bifurcation and a stable limit cycle is created (panel (D1)). As we move further inwards, the periodic orbit undergoes a process of spike-adding after another, which are the result of small loops that appear in the upper right part of the orbits (see panels (D2) and (D3)). We can see in panel (C) how at least eleven spikes are reached in the innermost region (see enlargement in panel (C1) to be able to observe the eleven spikes). If we continue further to the lower right region of the parameter space shown in (A), the process is reversed and occurs more rapidly: the orbit undergoes successive spike-deletion processes until it becomes a simple cycle that eventually disappears into new one Hopf bifurcation that makes the equilibrium stable again. Note that in the case of DG with $\tau_S = 1$ no chaos is detected, the maximum Lyapunov exponent is always zero (except when it converges to an equilibrium point where it is also negative).

For the MPR model, shown in Figure 4, the first and second maximum Lyapunov exponents are presented in the fig-
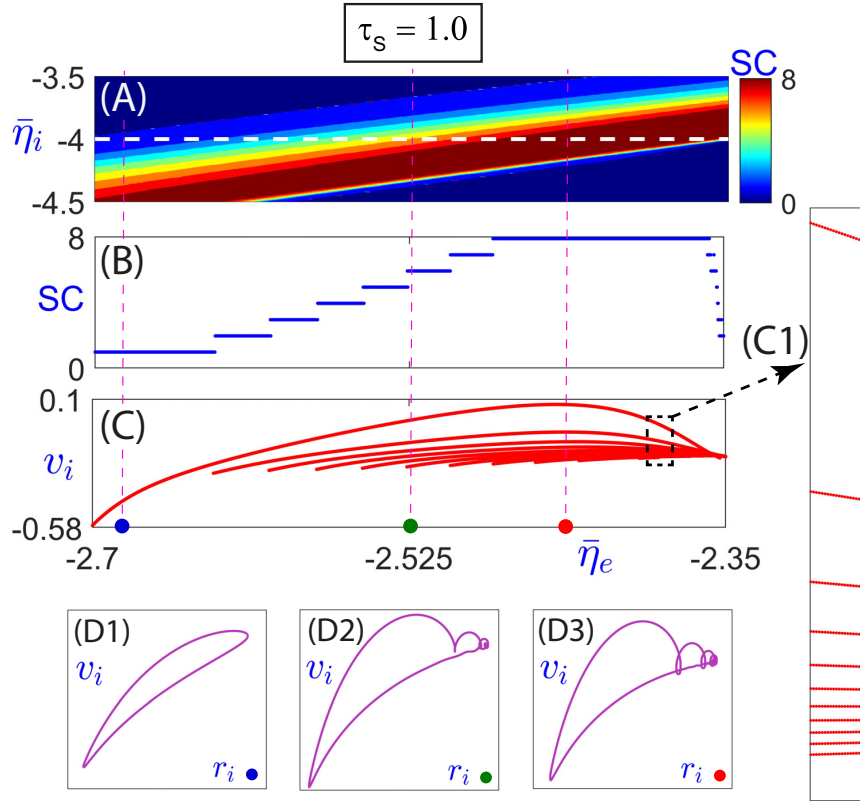
FIG. 3: Study of the behavior of the DG model for $\tau_S = 1$. (A) Biparametric spike-counting (SC) sweeping. The line corresponding to $\bar{\eta}_i = -4.0$, which is the one used for the rest of the graphs in this figure, is marked with a dashed white line. (B) Spike-counting sweeping along the dashed white line. (C) Poincaré section of the same line. (C1) Zoom of (C) to be able to see the eleven spikes. The transient time for all these panels is $3 \cdot 10^4$ ms and the integration time is 10^4 ms. (D1), (D2) and (D3) Orbits when $\bar{\eta}_i = -4.0$ and $\bar{\eta}_e$ is -2.673, -2.526 and -2.442, respectively.

ure in panel 4(B), in addition to the spike-counting plots. The first Lyapunov exponent is shown in yellow-orange when it is positive (i.e., for chaotic behavior), and the second Lyapunov exponent is shown in grayscale when the first is zero (i.e., for regular behavior). This image clearly shows the existence of large chaotic regions in the biparametric space. Note how both biparametric plots (panels Figure 4(A) and (B)) provide complementary information and the regions with the chosen maximum number of spikes correspond approximately to the chaotic regions. In the upper left and lower right regions, the attractor is again a point of equilibrium; and when advancing towards the inner zone it becomes unstable through a Hopf bifurcation that creates a stable cycle (panel (F1)). From here on, however, the processes that the attractor experiences are different from the previous case. Following the line $\bar{\eta}_i = -4.0$, we can observe how, at a value of $\bar{\eta}_e$ close to -2.64, a new spike appears (see panels (C) and (D)). This new spike corresponds to a small rise that occurs in the lower left part of the loop. In panel (G1), two periodic orbits are represented. The brown orbit is the attractor of $\bar{\eta}_e = -2.64$, and in this case there is only one point of intersection with the Poincaré section. On the other hand, the black orbit is the attractor when $\bar{\eta}_e = -2.63$, which already

has two cut-off points. Subsequently, for a value of $\bar{\eta}_e$ close to -2.62, a period-doubling bifurcation occurs (see brown orbit in panel (G2), $\bar{\eta}_e = -2.62$), so the two cuts that the orbit had before the bifurcation are now four. By further increasing the value of $\bar{\eta}_e$, one of the maxima of the variable v_i at the bottom is stretched until it no longer exists (see black orbit in panel (G2), $\bar{\eta}_e = -2.61$), which explains why in panels (C) and (D) it first goes from two to four spikes (at the period doubling bifurcation) and shortly after falls to three. In panel (G3), the orbit after the next period doubling bifurcation can be seen. Moving to the right on the line produces an infinite period-doubling cascade that causes the dynamics to become chaotic. The process is a little more complex than usual since, throughout this infinite period-doubling cascade, spike-adding and spike-deletion processes occur from time to time. The chaotic region ends with a fold bifurcation, where a new stable periodic orbit is born (which becomes an attractor), and an unstable one is also created. The above process is repeated numerous times along the line (as can be seen in panel (D)). Between the chaotic zones there are other zones of regular (periodic) behavior, some of them so narrow that they are not visible on the scale of the figure. Finally, upon exiting the inner region, the process will be reversed, dominating an
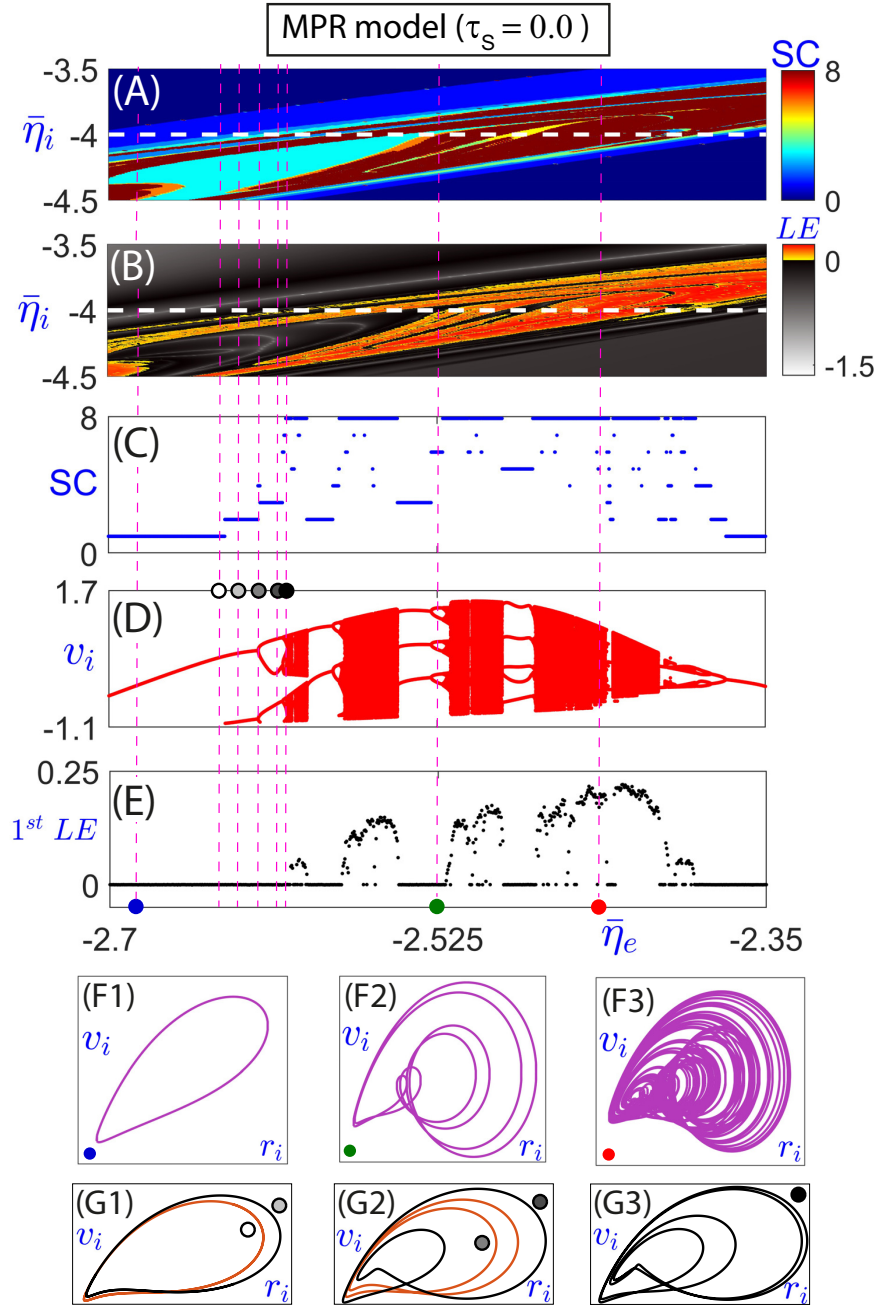
FIG. 4: Study of the behavior of the MPR model (DG model for $\tau_S = 0$). (A) and (B) Biparametric spike-counting (SC) and Lyapunov exponents (LEs), respectively. The line corresponding to $\bar{\eta}_i = -4.0$, which is the one used for the rest of the graphs in this figure, is marked with a dashed white line. (C) Spike-counting sweeping along the dashed white line. (D) Poincaré section of the same line. (E) Representation of the first Lyapunov exponent. The transient time for all these panels is $3 \cdot 10^4$ ms and the integration time is 10^4 ms. (F1), (F2) and (F3) Orbits when $\bar{\eta}_i = -4.0$ and $\bar{\eta}_e$ is -2.673, -2.526 and -2.442, respectively. (G1), (G2) and (G3) Orbits when $\bar{\eta}_i = -4.0$ and $\bar{\eta}_e = -2.64$, -2.63, -2.62, -2.61 and -2.607, respectively.

infinite period-halving cascade. The situation described along the line (and shown in panels (C)-(G)) is reproduced on the biparametric region shown in panels (A) and (B). There we can observe that there are several bands, of complex shape, where the dominant behavior is chaotic. These chaotic bands are surrounded by other regions of periodic behavior with an increasing number of loops as we move from the outside to the inside.

In conclusion, Figures 3 and 4 show in detail the dynamic differences of both models already hinted at in Figure 2. On the one hand, chaos appears in the MPR model, while it does not appear in the DG model with $\tau_S = 1$. On the other hand, the periodic orbits of both models with more than one spike are very different: the orbits of the MPR model have a funnel-
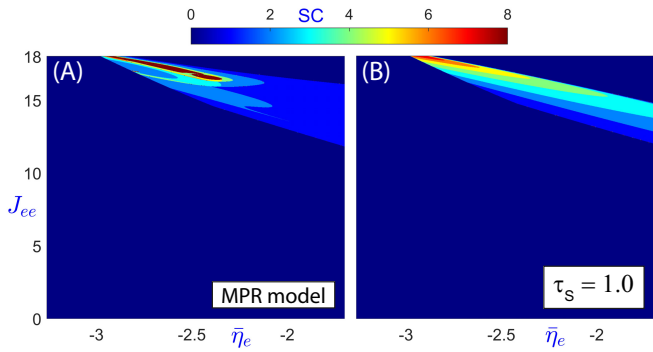
FIG. 5: (A) and (B) Biparametric spike-counting (SC) sweeping of MPR and DG model, respectively. The value of parameter $\bar{\eta}_i$ is set to -5.

like structure, while in the DG model (with $\tau_S = 1$) the dynamics are of bursting-type. These differences motivate the study of the dynamic properties of the DG model when τ_S changes from the value 0 (MPR model) to the value 1, with the aim of showing the transition between the observed dynamic behaviors.

Another question that arises is related to whether these dynamics are preserved by changing the coupling parameters J_*. To give a brief analysis we allow to change the value of the parameter J_{ee} (in the rest of the article J_{ee} is set to 18), and in Figure 5 we show the spike-counting sweeping in the biparametric plots $(\bar{\eta}_e, J_{ee})$ for the MPR and DG models. In both cases we have set the value of the parameter $\bar{\eta}_i = -5$. We observe how the richest dynamics is for $J_{ee} \in [12, 18]$, and, therefore, for this first analysis it is justified to use the value $J_{ee} = 18$ to study all the possible dynamics. It is open to perform a more exhaustive analysis to determine the global influence of all parameters.

Figure 6 presents biparametric plates for $\bar{\eta}_e \in [-3.26, -1.7]$, $\bar{\eta}_i \in [-5.94, -2.7]$ and for fixed values of $\tau_S \in [0, 3]$. Note that the parametric regions shown on these plates contain and expand those shown in panels (A) and (B) of Figure 4. Here we can see how the interior region seen in the previous ones with periodic or chaotic behavior is surrounded by the dark blue region that corresponds to an equilibrium point being the attractor and that is bounded by a Hopf bifurcation curve. By increasing τ_S from 0 to 0.05 we can see in the plates how the large chaotic zone has stretched and the bands are more evident. Furthermore, the small chaotic area at the bottom left has become much smaller. However, the regular zones are more similar, with the only difference that in the case $\tau_s = 0.05$, the zones left by the chaotic part are now regular. With $\tau_S = 0.075$, the changes described above continue: the chaotic region at the bottom left has completely disappeared and so have some of the upper bands, and the remaining chaotic areas are much thinner. For $\tau_S = 0.125$, no chaotic region is observed. Only three periodic regions (with 1, 2 and 3 loops from outside to inside) and the outer equilibrium region are present. From

here on, chaotic dynamics no longer appear for any value of the free parameters and the evolution process that we are going to observe when τ_S increases is different. In the inner region, new inner regions with more loops appear as we go deeper. Thus, for $\tau_S = 0.25$, the regions with 4 and 5 loops are visible; for $\tau_S = 0.375$ orbits with 6 and 7 loops also appear; and, from $\tau_S = 0.5$ onwards, there are orbits with 8 or more loops. Note that now the dark red region marks the maximum number of loops considered, and periodic orbits with a larger number of loops (but no chaotic attractor) exist. At the same time, we can see how the lower left tail becomes shorter and the upper right corner becomes more pointed. Furthermore, from $\tau_S = 1.0$ onwards, the region with periodic orbits with more than one loop becomes smaller, so with $\tau_S = 3.0$ a much smaller region is clearly observed and, although not shown in the figure, increasing τ_S even further, this region ends up disappearing, leaving only two possible behaviors, either convergence to an equilibrium point or a periodic orbit with a single loop.

All of the above figures have been made using a fixed set of initial conditions $(r_e, v_e, r_i, v_i, S_{ee}, S_{ei}, S_{ie}, S_{ii}) = (1, -1, 1, -1, 1, 1, 1, 1)$. However, different initial conditions can lead to different results in the case of multistability. To illustrate this situation we show in Figure 7 the spike-counting plots for the cases $\tau_S = 0$ and 1 of Figure 6 but now using random initial conditions and as a result noisy areas give us an idea of the regions with multistability. In fact, we have detected bistability. Graph (A1) provides an enlargement of a bistability region and, in the value of the red dot parameters, we show in graphs (A2) and (A3) the two possible orbits. Case (A2) is the standard spiking-like (phase-locked) orbit and case (A3) is an orbit with a long transient that eventually reaches an equilibrium point. Therefore, bistability is present, but no new dynamics are observed, so for this study we continue with our set of initial conditions.

In Figure 8 we combine all the plates in Figure 6 into a single three-dimensional image. In addition, we include a plate with $\tau_S = 10$ that shows the continuity of the dynamic properties described up to $\tau_S = 3$, as well as a plate with constant $\bar{\eta}_e = -2.41$, and $\bar{\eta}_i$ and τ_S as free parameters that intersect all other plates. Three main types of attractors are detected in the DG model: a funnel-type (periodic or chaotic) orbit (as seen in the classical Rössler model), shown in panel (C1); a bursting-type periodic orbit, in panel (C2); and a simple cycle that generates spiking dynamics, in panel (C3). Panel (B) schematically shows the distribution of attractors in the space of three parameters. The spiking dynamics is ubiquitous for any value of τ_S. On the other hand, Rössler-type orbits only appear for values τ_S close to 0 and bursting-type orbits for values close to 1. At intermediate values the division is not so clear. As an example of this, panel (D) shows several time series of attractors at a point with regular dynamics for different values of τ_S. We can see how the time series are gradually deformed as the value of τ_S increases to go from one type of dynamics to another.

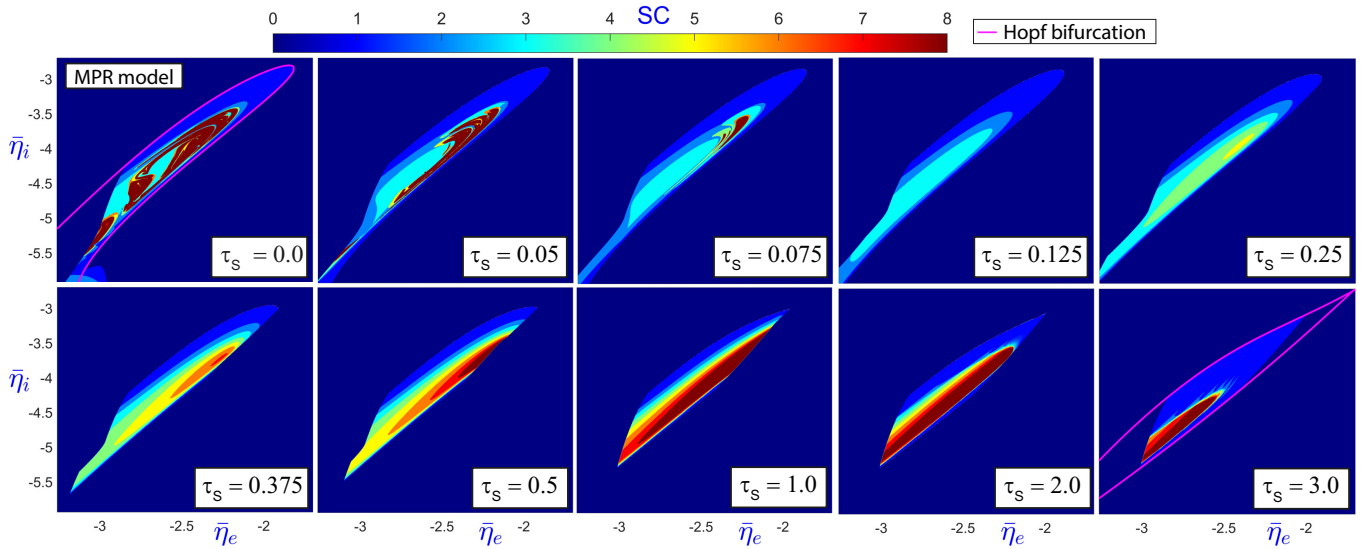In summary, in this article we have analyzed the influence

FIG. 6: Spike-counting sweeping (see upper color bar) of a biparametric region when the parameter τ_S of the DG model (2) varies between 0 (corresponding to the MPR model (1)) to 3. The Hopf bifurcation is marked in pink on the extreme value plots. The transient time for all these panels is $3 \cdot 10^4$ and the integration time is 10^4. The initial conditions are $(r_e, v_e, r_i, v_i, S_{ee}, S_{ei}, S_{ie}, S_{ii}) = (1, -1, 1, -1, 1, 1, 1, 1)$.

of the synaptic adaptation mechanism on the macroscopic dynamics of coupled neural populations (through coupled next-generation neural masses [38] that exactly reproduce the dynamics of fully coupled networks of quadratic integrate-and-fire spiking neurons). This low-dimensional mean-field reduction has allowed the analysis of different types of macroscopic dynamics.

We have shown that there are three main dynamical regimes in coupled models: Rössler-type, bursting-type, and spiking-type (oscillator-type) dynamics. In the publications [9, 18] the existence of bursting-type and oscillator-type dynamics was already detected, but we added the case of chaotic dynamics and also studied the parametric distribution of the different dynamics. This result opens the question of which regime is more suitable for realistic simulations of large neural networks and the differences between using or not using adaptation mechanisms. We highlight that we have detected the possibility of the appearance of chaotic collective dynamics when synaptic adaptation is very weak (or not present). This result may motivate experiments, using cholinergic or similar drugs to reduce synaptic adaptation, to actually observe whether this is the case in nature. Furthermore, it is part of our future research to study in detail all the dynamic mechanisms of creation and destruction of the different dynamics in the parameter space.

APPENDIX

Neural population equations

The coupled populations are formed by QIF neurons that are described by the voltages v_j whose evolution is studied using the following equation in the case of MPR model [17]:

$$\dot{v}_{e,j} = v_{e,j}^2 + \eta_{e,j} + J_{ee}r_e - J_{ei}r_i + I_e^{ext}, \qquad (A.1)$$

for the neurons of the excitatory population where $j = 1, ..., N_e$ and

$$\dot{v}_{i,j} = v_{i,j}^2 + \eta_{i,j} + J_{ie}r_e - J_{ii}r_i + I_i^{ext}, \qquad (A.2)$$

for the inhibitory ones where $j = 1, ..., N_i$. Notice that r_e and r_i are the firing rates of the excitatory and inhibitory populations, respectively; $(J_{ee}, J_{ei}, J_{ie}, J_{ii})$ are the synaptic strengths of the connections; $(\eta_{e,j}; \eta_{i,j})$ are the Lorentzian distributed constant currents defining the intrinsic resting potential and firing threshold of the neurons and (I_e^{ext}, I_i^{ext}) are the external inputs.

In the case of DG model, the voltages v_j of QIF neurons of both populations are given by the following equations [7]:

$$\begin{aligned}
\tau_e \dot{v}_{e,j} &= v_{e,j}^2 + \eta_{e,j} + \tau_e S_{ee} - \tau_e S_{ei} + I_e^{ext}, \\
\tau_i \dot{v}_{i,j} &= v_{i,j}^2 + \eta_{i,j} + \tau_i S_{ie} - \tau_i S_{ii} + I_i^{ext},
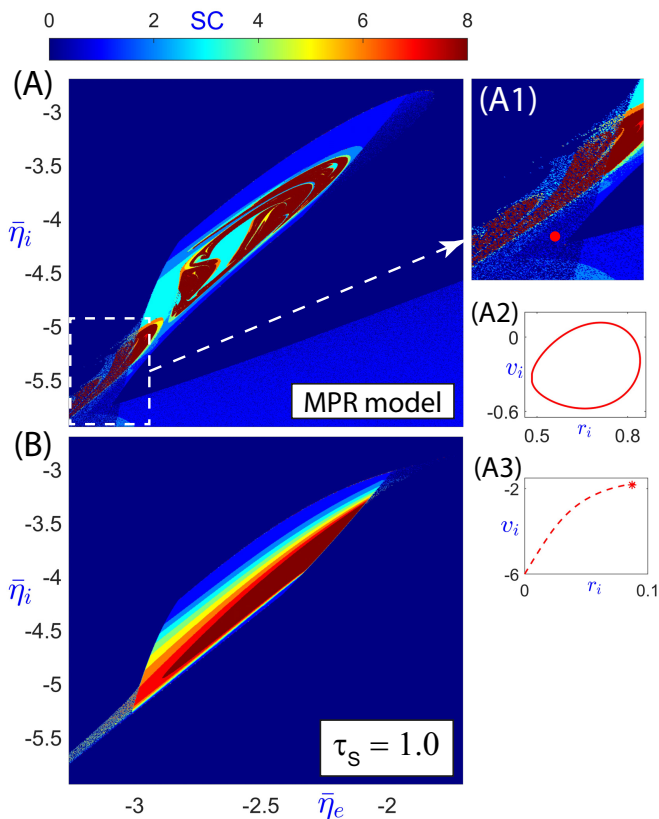\end{aligned} \qquad (A.3)$$

FIG. 7: Study of spike-counting (SC) sweeping using random initial conditions. (A) and (B) Biparametric spike-counting sweeping of the MPR and DG model, respectively. The random initial conditions of r_e and r_i belong to $[0,1]$, and v_e and v_i to $[-2,2]$ (the initial conditions of the synaptic currents are fixed as 1). (A1) Zoom of (A) to notice the bistability. The red dot corresponds to $\bar{\eta}_e = -3.114077135603254$ and $\bar{\eta}_i = -5.7$. With these parameter values and using the initial conditions $(1,-1,1,-1)$ the orbit (A2) is obtained, and with the initial conditions $(0,0,0,-6)$ the orbit (A3) is obtained.

where $j = 1,...,N_e$ in the first equation and $j = 1,...,N_i$ in the second one. Moreover, τ_e and τ_i are the membrane time constants (the other parameters have been explained in MPR model) and the synaptic currents between the connections $(S_{ee}, S_{ei}, S_{ie}, S_{ii})$ are described as follows:

$$\begin{aligned}
\tau_{S_e}\dot{S}_{ee} &= -S_{ee} + J_{ee}r_e, \\
\tau_{S_e}\dot{S}_{ie} &= -S_{ie} + J_{ie}r_e, \\
\tau_{S_i}\dot{S}_{ei} &= -S_{ei} + J_{ei}r_i, \\
\tau_{S_i}\dot{S}_{ii} &= -S_{ii} + J_{ii}r_i,
\end{aligned} \qquad (A.4)$$

where τ_{S_e} and τ_{S_i} are the synaptic time constants of the connections (and the other parameters have been explained before).

We have to take into account that when $v_{*,j} \geq v_{th}$, that is, when the value of the voltage crosses the threshold v_{th}, then $v_{*,j} = v_r$ (the value of the voltage returns to the reset value v_r). We consider that $v_{th} = -v_r \to \infty$ to capture the spike reset as well as the refractory time of the neuron. In numerical

simulations a finite value for v_{th}, and consequently for v_r, is used. In our simulations $v_{th} = -v_r = 100$.

To achieve the heterogeneity of the network, parameter η_* ($* \in \{e,i\}$) is distributed randomly using Lorentzian distribution [16]:

$$\mathcal{L}(\eta_*) = \frac{\Delta_*}{\pi[(\eta_* - \bar{\eta}_*)^2 + \Delta_*^2]},$$

where Δ_* and $\bar{\eta}_*$ are the half-width and the mean value (in the Cauchy sense) of the named distribution. In the simulations of the whole network, given the values of Δ_* and $\bar{\eta}_*$, the values of $\eta_{*,j}$ (for each neuron of each population) is computed as follows [16]:

$$\eta_{*,j} = \bar{\eta}_* + \Delta_* \tan\left(\frac{\pi(2j - N_* - 1)}{2(N_* + 1)}\right), \qquad (A.5)$$

for $j = 1,...,N_*$ ($* \in \{e,i\}$). Notice that neuron j of population $*$ is excitable if $\eta_{*,j}$ is negative; and neuron j is firing tonically and emits a regular train of spikes when $\eta_{*,j}$ is positive.

In Table I, the units of the variables and parameters are indicated (symbol - in the units column, means that the parameter is dimensionless). Moreover, the initial conditions of the variables and the values of the parameters used in the figures (unless otherwise indicated) are shown. Notice that the models MPR and DG have been obtained using the QIF model which is not a biological one, it is a theoretical model that reproduces the main dynamics of the populations behavior. This model is obtained from the normal form of the Saddle-Node bifurcation and, therefore, it is dimensionless for $\dot{v}_e$ and $\dot{v}_i$.

	Units	Values
r_e, r_i	1/ms	Initial conditions: 1,1
v_e, v_i	mV	Initial conditions: -1,-1
$S_{ee}, S_{ei}, S_{ie}, S_{ii}$	1/ms	Initial conditions: 1,1,1,1
τ_e, τ_i	ms	1,1
τ_{S_e}, τ_{S_i}	ms	$[0,10],[0,10]$
Δ_e, Δ_i	-	1,1
$\bar{\eta}_e, \bar{\eta}_i$	-	$[-3.26,-1.7],[-5.94,-2.7]$
I_e^{ext}, I_i^{ext}	A	0,0
$J_{ee}, J_{ei}, J_{ie}, J_{ii}$	-	$18,6,18,0$

TABLE I: Units of the variables (and their initial conditions) and parameters (and their values) used for the MPR and DG models (unless otherwise indicated)-

Numerical techniques

In the simulations of the whole network, to obtain the plots of Figure 1 (corresponding to MPR model), we have taken $50,000$ neurons for the excitatory population and the same number for the inhibitory population. Therefore, we have to solve $100,000$ ordinary differential equations given by (A.1) and (A.2) using a Runge-Kutta integrator of order 5 (with time step 0.001 and saving every 10 steps). The threshold of the
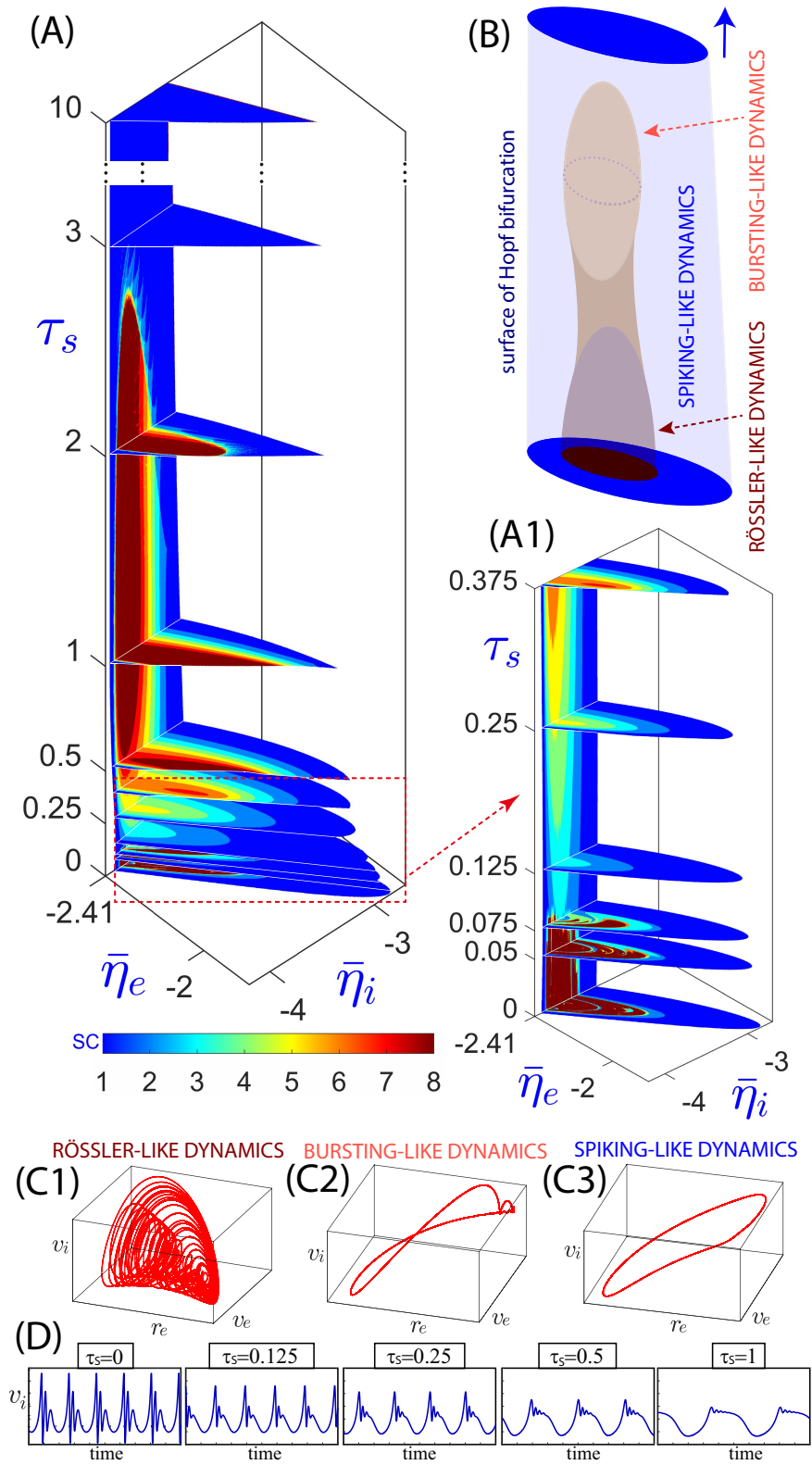
FIG. 8: Spike-counting (SC) sweeping when three parameter values are changed, and plot of some orbits for different values of τ_S. The transient time used for all these panels is $3 \cdot 10^4$ and the integration time is 10^4. (A) and (A1) Spike-counting sweeping of the graphs of Figure 6 (and the corresponding one for $\tau_S = 10$) and of the biparametric region $(\bar{\eta}_i, \tau_S)$ with $\bar{\eta}_e = -2.41$. (B) Scheme of the different dynamics that occur when the parameter τ_S changes. (C1), (C2) and (C3) Representation of the orbits in the three different zones shown in (B). The value of the parameter τ_S is 0, 1 and 3, respectively, and $\bar{\eta}_e = -2.41$ and $\bar{\eta}_i = -3.9$ for the three plots . (D) Time series for the attractor with different values of τ_S ($\bar{\eta}_e = -2.54$ and $\bar{\eta}_i = -4.0$)

voltage is $v_{th} = 100$ (as in [17]) and therefore, $v_r = -100$. The values of the parameters used for the simulations are $\Delta_e = \Delta_i = 1$, $\bar{\eta}_e = -2.526$, $\bar{\eta}_i = -4$, $J_{ee} = J_{ie} = 18$, $J_{ei} = 6$, $J_{ii} = 0$ and $I_e = I_i = 0$. The initial condition for all the variables is set to 0.

To obtain the plots corresponding to the mean-field equations (MPR model) in Figure 1, we have used the equations of (1). Then, we have solved a system of four ordinary differential equations using a Runge-Kutta integrator of order 5 (time step 0.0001).

For the simulations of the whole network of DG model the equations of (A.3) and (A.4) (using (A.5) to obtain the values of $\eta_{*,j}$) are used. To obtain the time series of DG model the equations of (2) are integrated.

The spike-counting technique [37] (also called isospike technique [39]) consists on selecting a Poincaré section or to impose a suitable condition (like to detect all the relative maxima of the orbit, what is the condition used in this article). And later, after a long transient integration to go to the asymptotic invariant, we use the selected condition to compute the corresponding points to detect the period and maxima (in our case) for the periodic case, or to put the maximum number of allowed points that means or chaotic behavior or a very long periodic orbit. In order to represent the different dynamics a color is assigned to each number of maxima. To obtain the spike-counting plots of Figures 3, 4, 5, 6, 7 and 8 we use the advanced capabilities of the Taylor series numerical integrator TIDES [40] that allows a continuous output, very suitable for the location of the maxima points of the orbits.

The Runge-Kutta integrator of order 5 (with time step 0.001) is applied to obtain the time series that we need in the algorithm in [41] used to compute (an approximation of) the Lyapunov exponents.

––––––––––

* Electronic address: rbarrio@unizar.es; CODY group: http://cody.unizar.es

[1] G. Buzsáki, *Rhythms of the Brain* (Oxford University Press, 2006).

[2] D. Pazó and E. Montbrió, Phys. Rev. Lett. **116**, 238101 (2016).

[3] P. Ashwin, S. Coombes, and R. Nicks, The Journal of Mathematical Neuroscience **6**, Article 2 (2016).

[4] G. Dumont, G. B. Ermentrout, and B. Gutkin, Phys. Rev. E **96**, 042311 (2017).

[5] C. Bick, C. Laing, M. Goodfellow, and E. Martens, Journal of Mathematical Neuroscience **10**, 1 (2020).

[6] C. Bick, M. Goodfellow, C. Laing, and E. A. Martens, J. Math. Neurosc. **10**, Article number: 9 (2020).

[7] G. Dumont and B. Gutkin, PLOS Computational Biology **15**, e1007019 (2019).

[8] D. Reyner-Parra and G. Huguet, PLOS Computational Biology **18**, e1009342 (2022).

[9] A. Ferrara, D. Angulo-Garcia, A. Torcini, and S. Olmi, Phys. Rev. E **107**, 024311 (2023).

[10] P. Fries, Annual Review of Neuroscience **32**, 209 (2009).

[11] P. Fries, Trends in cognitive sciences **9**, 474 (2005).

[12] H. A. Swadlow and S. G. Waxman, Scholarpedia **7**, 1451 (2012).

[13] E. Maris, P. Fries, and F. van Ede, Trends in neurosciences **39**, 86 (2016).

[14] E. Lowet, M. Roberts, A. Hadjipapas, A. Peter, J. van der Eerden, and P. De Weerd, PLoS computational biology **11**, e1004072 (2015).

[15] C. C. Canavier, Current opinion in neurobiology **31**, 206 (2015).

[16] H. Taher, *Next generation neural mass models: working memory, all-brain modelling and multi-timescale phenomena*, Ph.D. thesis, Université Côte d'Azur (2021).

[17] E. Montbrió, D. Pazó, and A. Roxin, Physical Review X **5**, 021028 (2015).

[18] A. Ceni, S. Olmi, A. Torcini, and D. Angulo-Garcia, Chaos: An Interdisciplinary Journal of Nonlinear Science **30**, 053121 (2020).

[19] J. Sawicki, R. Berner, S. A. M. Loos, M. Anvari, R. Bader, W. Barfuss, N. Botta, N. Brede, I. Franović, D. J. Gauthier, S. Goldt, A. Hajizadeh, P. Hövel, O. Karin, P. Lorenz-Spreen, C. Miehl, J. Mölter, S. Olmi, E. Schöll, A. Seif, P. A. Tass, G. Volpe, S. Yanchuk, and J. Kurths, Perspectives on adaptive dynamical systems (2023), arXiv:2303.01459 .

[20] R. Barrio, M. Angeles Martínez, S. Serrano, and A. Shilnikov, Chaos: An Interdisciplinary Journal of Nonlinear Science **24** (2014).

[21] S. Olmi, R. Livi, A. Politi, and A. Torcini, Phys. Rev. E **81**, 046119 (2010).

[22] M. Whittington, R. Traub, and J. Jefferys, Nature **373**, 612–615 (1995).

[23] F. Devalle, A. Roxin, and E. Montbrió, PLOS Computational Biology **13**, 1 (2017).

[24] S. P. Aiken, B. J. Lampe, and B. S. Brown, British Journal of Pharmacology **115**, 1163 (1995).

[25] R. D. Traub, R. Miles, and G. Buzsáki, The Journal of Physiology **451**, 653 (1992).

[26] S. M. Crook, G. B. Ermentrout, and J. M. Bower, Neural Computation **10**, 837 (1998).

[27] E. L. Newman, S. N. Gillet, J. R. Climer, and M. E. Hasselmo, Journal of Neuroscience **33**, 19635 (2013).

[28] W. M. Howe, H. J. Gritton, N. A. Lusk, E. A. Roberts, V. L. Hetrick, J. D. Berke, and M. Sarter, Journal of Neuroscience **37**, 3215 (2017).

[29] E. Ott and T. M. Antonsen, Chaos: An Interdisciplinary Journal of Nonlinear Science **18**, 037113 (2008).

[30] M. Woodman and C. Canavier, J Comput Neurosci **31**, 401–418 (2011).

[31] S. Wang, L. Chandrasekaran, F. R. Fernandez, J. A. White, and C. C. Canavier, PLOS Computational Biology **8**, 1 (2012).

[32] G. Weerasinghe, B. Duchet, H. Cagnan, P. Brown, C. Bick, and R. Bogacz, PLOS Computational Biology **15**, 1 (2019).

[33] B. Jüttner, C. Henriksen, and E. A. Martens, Chaos: An Interdisciplinary Journal of Nonlinear Science **31**, 023141 (2021).

[34] O. Rössler, Physics Letters A **57**, 397 (1976).

[35] R. Barrio, F. Blesa, and S. Serrano, Physica D: Nonlinear Phenomena **238**, 1087 (2009).

[36] R. Barrio, S. Ibáñez, L. Pérez, and S. Serrano, Chaos: An Interdisciplinary Journal of Nonlinear Science **31**, 043120 (2021).

[37] R. Barrio and A. Shilnikov, The Journal of Mathematical Neuroscience **1**, 1 (2011).

[38] S. Coombes, Frontiers in Applied Mathematics and Statistics **9**, Article 112822 (2023).

[39] J. G. Freire and J. A. C. Gallas, Phys. Chem. Chem. Phys. **13**, 12191 (2011).

[40] A. Abad, R. Barrio, F. Blesa, and M. Rodríguez, ACM Transactions on Mathematical Software (TOMS) **39**, 1 (2012).

[41] A. Wolf, J. B. Swift, H. L. Swinney, and J. A. Vastano, Physica D: nonlinear phenomena **16**, 285 (1985).